EPJ Applied Metamaterials

RESEARCH ARTICLE

OPEN ⓐ ACCESS

Multiresonant metasurface for Raman spectroscopy beyond single molecule detection level

Saeid Izadshenas[1,*] ⓘ, Piotr Masłowski[1], Tobias Herr[2,3], and Karolina Słowik[1]

[1] Institute of Physics, Faculty of Physics, Astronomy and Informatics, Nicolaus Copernicus University in Torun, ul. Grudziądzka 5, 87–100 Torun, Poland
[2] Deutsches Elektronen-Synchrotron DESY, Notkestr. 85, 22607 Hamburg, Germany
[3] Physics Department, Universität Hamburg UHH, Luruper Chaussee 149, 22761 Hamburg, Germany

Abstract. A metasurface in the metal-insulator-grating configuration is designed and optimised to support enhancement of coherent Raman signal of selected molecules orders of magnitude above the single-molecule detection threshold. The tunability is demonstrated by adjusting the structure to match selected Raman peaks of rhodamine, however, its spectral response is broad enough to cover a range of Raman shifts. Finally, the grating allows switching between distinct values of Raman shift with a single metasurface illuminated at different angles.

Keywords: metasurface / coherent anti-stokes Raman scattering / surface plasmon / plasmonic grating / molecular spectroscopy

1 Introduction

Raman spectroscopy allows detection and identification of different molecular species even in complex samples with relatively simple experimental setups. Raman techniques can be used on various types of samples, and the spectra can be acquired in short times and from small, even microscopic volumes [1]. However, the major drawback of the technique is the typically weak signal, that makes the approach inefficient especially for low concentration, for example in bio-medical diagnostics. Enhancement of the Raman signal at nanostructured metallic surfaces [2,3] allowed lowering the detection threshold to extremely low concentrations, making sensing at the level of single molecules possible [4–6]. However, operation at such low concentrations remains challenging and requires tip-enhanced spectroscopy techniques [5,7–9] or novel dedicated microscope designs [10]. Further improvement of sensitivity is still needed, on the one hand, to relax these requirements. On the other hand, greater sensitivity would allow extending the range of detected molecular species, or would even enable identification of single unknown molecules. A potential to achieve these ambitious goals is offered by the coherent anti-Stokes Raman scattering (CARS) technique, that exploits a nonlinear four-wave mixing process [11–13]: Two beams, referred to as pump and Stokes beams of frequencies ω_p and ω_s coherently interact and, as a result, give rise to a coherent signal at the anti-Stokes frequency ω_a under the resonance condition that corresponds to the energy conservation requirement

$$\omega_p - \omega_s = \omega_a - \omega_p = \Delta, \quad (1)$$

where the Raman shift Δ is a characteristic feature of a given molecule related to its vibronic profile (Fig. 1). Surface enhanced CARS (SECARS) additionally exploits signal intensity enhancement related to occurrence of plasmonic excitations at the surface of metallic nanoparticles: these nanoparticles can be tailored in order to locally enhance electromagnetic fields of desired optical to near-infrared frequencies [14]. Still, engineering particles that would simultaneously enhance electric fields at multiple desired frequencies is in general a challenging task. The SECARS technique can be significantly more sensitive than the standard surface-enhanced Raman spectroscopy [15]. In order to achieve single-molecule sensitivity, huge signal enhancement is required of at least 10–11 orders of magnitude [4]. With exactly this performance level, exploiting two broad plasmonic modes resonant with the Stokes and anti-Stokes field, the technique has already been demonstrated to enable molecular detection at the single-molecule level [16,17]. Plasmonic nanostructures with even stronger predicted enhancement have been engineered such as gold trimers [18] or silver metal-insulator-metal configurations [19].

Here, we make a contribution towards exploring the potential of plasmonic enhancement of CARS in greater depth, and propose a metal-insulator-grating metasurface that

---

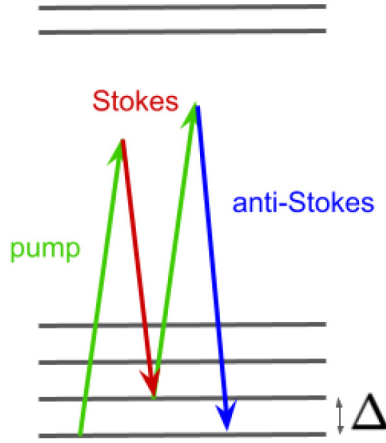* e-mail: s.izadshenas@doktorant.umk.pl

Fig. 1. Scheme of the coherent anti-Stokes Raman scattering event: an absorption of two photons of the probe beam along with a stimulated emission of a photon in the Stokes beam results in a coherent emission of a photon at the anti-Stokes frequency. Black lines represent molecular energy levels, e.g., associated with its vibrational structure. Note that the sample is illuminated with two, pump and Stokes fields, while the anti-Stokes radiation is generated through the nonlinear process.

supports multiple, tunable resonance peaks. Similar structures have been investigated before in the context of tunable multi-resonant optical response [20,21]. We base the design on gold elements, which is generally more stable in experimental conditions than silver that performs better in theory leading to stronger enhancement predictions. The structure unit cell combines a nanodisk dimer and a grating: three elements which, when coupled, support three resonance modes in the near-infrared regime of interest. In particular, each of the disks supports a peak corresponding to its fundamental resonance. Their coupling leads to the resonance splitting in a pair. This pair will give rise to the Stokes and anti-Stokes peaks, however, influenced by the presence of grating. That allows us to shift the pair in the spectral domain and achieve tunability by modification of the incidence angle of illuminating beams. Additionally, the grating sharpens the Stokes and anti-Stokes pair and gives rise to a third resonance that will play the role of the pump peak. To demonstrate the potential to tailor the metasurface by design to match the Raman profiles of various molecules, we adjust the geometry parameters to selected peaks in the Raman spectrum of rhodamine 6G. Finally, we demonstrate how the same structure could be tuned post fabrication to match other values of Raman shift.

2 Metasurface geometry CARS signal enhancement of rhodamine

A unit cell of the metasurface under consideration is schematically depicted in Figure 2a (side view) and Figure 2b (top view). We exploit the metal-insulator-grating (MIG) arrangement. In the top layer, each unit cell contains two coupled gold nanodisks of the same radius R and height h_d, separated by a gap of size d. A gold grating with each slab of width w_g and height h_g extended in the y direction makes the bottom layer. The slabs are separated by gaps of size g. A glass (SiO$_2$) insulator spacer slab of height h_s is sandwiched in

between as the middle layer. In the xy plane, the unit cell has a square shape of side length P. The surrounding medium is air. The structure could be fabricated in a bottom up scenario, where subsequent layers could be structured by electron beam lithography.

This choice of a metasurface offers a rich multi-resonant optical spectrum with three peaks in the near-infrared regime that can be tuned by design to match the Raman profile of a molecule of choice (see example spectra in Fig. 3 and below for a detailed discussion). Each of the nanodisks plays the role of an electric dipole, and their coupling gives rise to a pair of resonances. The third peak results from coupling the nanodisks with the grating. Naturally, in the miniaturized structure, all geometry parameters affect the spectral positions of each of these resonances. However, to the first approximation, we can spectrally tune the side peaks modifying the disks while changing the grating pattern mostly affects the middle resonance (see Appendix A).

The geometry parameters of the unit cell are engineered to match prominent Raman peaks of rhodamine 6G at $\Delta_1 = 1314\,\mathrm{cm}^{-1}$, $\Delta_2 = 1363\,\mathrm{cm}^{-1}$ and $\Delta_3 = 1512\,\mathrm{cm}^{-1}$ [22,23]. Optimisation of the structure for each value of the Raman shift corresponds in general to a whole new design, where modification of the geometry parameters allows for tuning the three peak positions of the spectral response to match the CARS resonance condition (1) for a given Δ_j. The design is performed numerically, by solving full-vectorial Maxwell's equations in the frequency domain with the finite integration technique, using the commercial solver CST Studio Suite.

Periodic boundary conditions in x and y directions are used to extend the unit cell of the metasurface. For the SiO$_2$ insulator, we have set the refractive index $n = 1.45$ [24], and Palik's data were used to model the dielectric permittivity of gold [25] in the two nanodisks and the grating. The metasurface is illuminated with a plane wave incident in the z direction from the top (disk) side with electric and magnetic fields polarised in the x and y directions, respectively. Default surface-based tetrahedral meshing was chosen in the numerical study. The number of mesh cells was 230638, with the cell per max model box edge was 10. The length of the shortest and longest edge was 2.5 nm and 255.399 nm, respectively. The minimum and maximum of all mesh cell quality values were 0.071 and 0.998, respectively. Matching the metasurface with a given value of the Raman shift Δ_j is based on variation of metasurface geometry parameters, and here, adjustment of the gaps d between the disks and g between the grating slabs plays the key role. With fixed thicknesses of all elements: $h_d = 35$ nm, $h_s = 250$ nm, $h_g = 30$ nm, fixed disk radius $R = 90$ nm, grating width $w_g = 20$ nm and unit cell size $P = 600$ nm, the gap sizes can be adjusted to match any of the three rhodamine Raman shifts given above. The resonant values are collected in the 3rd and 4th columns of Table 1.

We now investigate in greater detail the optical response of the metasurface for the set of geometry parameters corresponding to the Raman shift $\Delta_1 = 1314\,\mathrm{cm}^{-1}$. The setup sustains the required multi-resonant character, as evident from the reflection $R(\lambda)$, transmission $T(\lambda)$ and absorption $A(\lambda) = 1 - R(\lambda) - T(\lambda)$ spectra in Figure 3, where λ stands for the free-space wavelength. The three peak positions in the near-infrared are given in Table 1 in terms of the
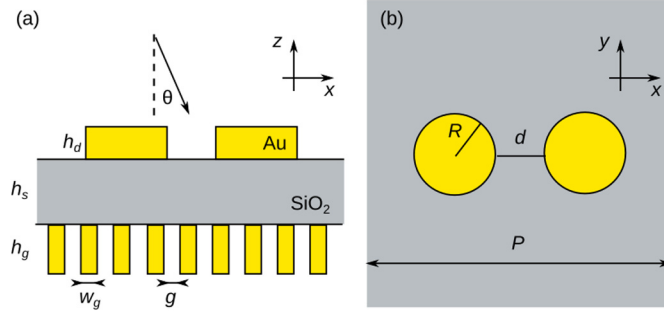
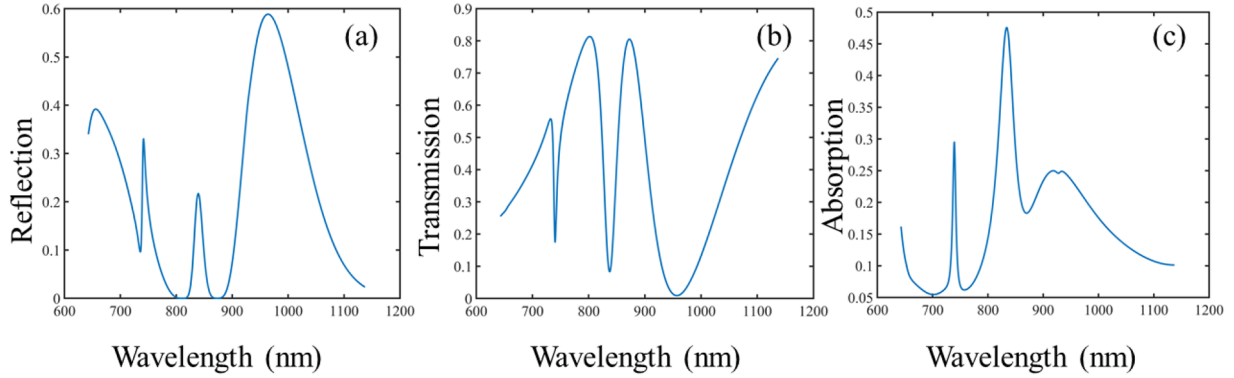**Fig. 2.** Unit cell of the proposed metasurface: side (a) and top (b) views.

Fig. 3. Spectra of the MIG metasurface with geometry arrangements matching the rhodamine 6G Raman shift $\Delta_1 = 1314$ cm^{-1}: (a) reflection, (b) transmission and (c) absorption.

Table 1. Geometry parameters (d, g) for which the spectral response of the investigated metasurface adjusts to different rhodamine 6G Raman shifts Δ_j, resonance positions of the resulting peaks in the metasurface spectral response $\lambda_{s,p,a}^j$, maximum value of the corresponding local scattered field enhancement factors at peak wavelengths $FE(\lambda_{s,p,a}^j) \equiv FE(\vec{r}_{\max}, \lambda_{s,p,a}^j)$, and the maximum value of the local SECARS enhancement factor $G_{SECARS}^{\Delta_j}$. Maximization is here performed over positions within the unit cell.

		Geometry		Stokes		Pump		Anti-Stokes		G^{Δ_j}
Δ_j [cm^{-1}]		d [nm]	g [nm]	λ_s^j [nm]	$FE(\lambda_s^j)$	λ_p^j [nm]	$FE(\lambda_p^j)$	λ_a^j [nm]	$FE(\lambda_a^j)$	
$j=1$	1314	7.4	5.4	920	81	821	71	741	28	1.3×10^{14}
$j=2$	1363	7.5	5.5	930	79	825	69	742	25	1.1×10^{14}
$j=3$	1512	10.0	5.6	939	82	822	55	731	18	0.2×10^{14}

corresponding peak wavelengths $\lambda_{S;p;a} = 2\pi c / \omega_{S;p;a}$, where c is the vacuum speed of light and we refer to the lowest-, mid- and highest-energy resonances respectively as the Stokes, pump and anti-Stokes. The peak wavelengths fulfill the CARS resonance condition (1).

The spectra in Figure 3 are related to the local electric field enhancement factors

$$FE(r, \lambda) = \frac{\left| \vec{E}(\vec{r}, \lambda) \right|}{\left| \vec{E}_0 \right|}, \qquad (2)$$

where $\vec{E}(\vec{r}, \lambda)$ corresponds to the scattered electric field at position $\vec{r}$ in the unit cell for illumination at the wavelength λ with a plane wave of amplitude $\left| \vec{E}_0 \right|$. In general, the field

enhancement factor depends on polarisation of the illuminating beam, which we here set parallel to the x direction as indicated above. Please note that frequency conversion effects in gold nanostructures are relatively inefficient and the corresponding signal would not be expected to spectrally overlap with the Raman signal.

The near-field distributions for resonant illumination at the Stokes, pump and anti-stokes wavelengths are presented in Figure 4, where the absolute value of the electric field amplitude normalized to the input field is shown in the xy plane directly above the nanodisks. Regions of strong electric field enhancement for different illumination wavelengths overlap, promising high local SECARS enhancement. Also, the points of maximum electric field enhancement $\vec{r}_{\max}$ occur in the gap region between the
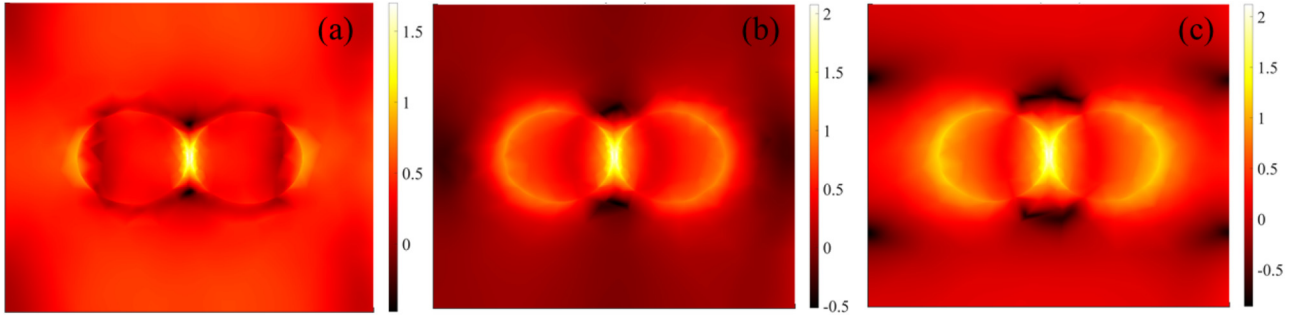
Fig. 4. The near field amplitude enhancement distributions $log_{10}\left[FE(\vec{r}, \lambda_{a,p,s}^1)\right]$ across the unit cell, in the plane directly above the nanodisks at the wavelengths corresponding to the (a) anti-stokes (741 nm), (b) pump (821 nm), and (c) stokes (920 nm) peaks.
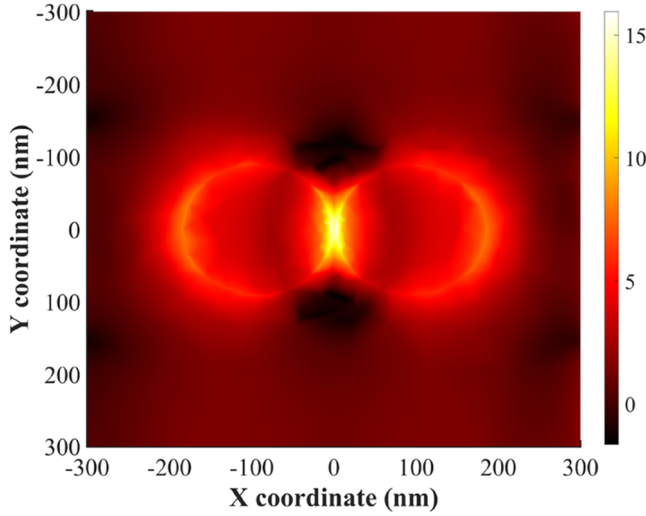

Fig. 5. Distribution of the SECARS enhancement factor $log_{10}G^{\Delta_1}(\vec{r}, \lambda_S^1, \lambda_p^1, \lambda_a^1)$ across the unit cell directly above the nanodisk top surface.
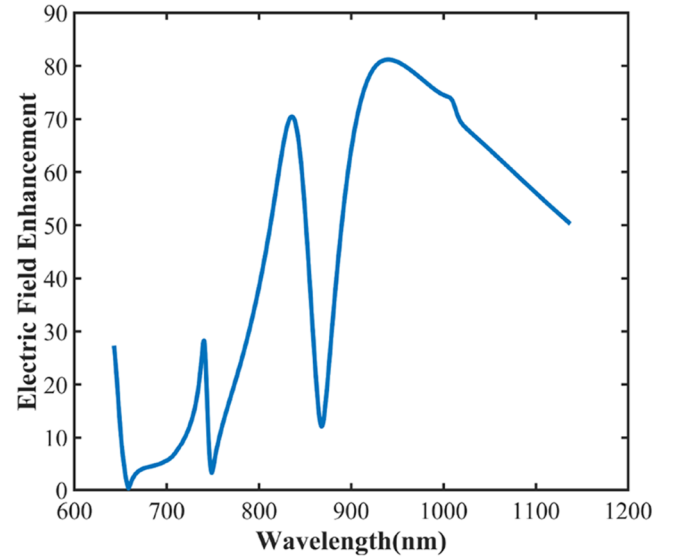

Fig. 6. Electric field enhancement factor $FE(\vec{r}_{\max}, \lambda)$ at the position of strongest enhancement $\vec{r}_{\max}$ in the nanodisk gap as a function of the free space illumination wavelength λ.

disks for all three wavelengths. This means that a rhodamine molecule positioned in a hotspot generated in the nanodisk gap would be subject to a significantly enhanced field that would give rise to a strong CARS signal.

In quantitative terms, local SECARS enhancement factor is evaluated as a product of the field enhancement factors in accordance with the nonlinear four wave mixing scheme depicted in Figure 1

$$G(r, \lambda_s, \vec{\lambda}_p, \lambda_a) = FE(\vec{r}, \lambda_s)^2 \cdot FE(\vec{r}, \lambda_p)^4 \cdot FE(\vec{r}, \lambda_a)^2. \tag{3}$$

Below we will denote as $G^{\Delta_1}(\vec{r}, \lambda_s, \lambda_p, \lambda_a)$ the value of the enhancement provided by the metasurface optimised to match the Raman shift Δ_1 in accordance with Table 1. The metasurface under consideration gives rise to the local SECARS enhancement factor of maximum value $G^{\Delta_1}(\vec{r}_{max}, \lambda_S^1, \lambda_p^1, \lambda_a^1) \approx 1.3 \times 10^{14}$. Geometries optimised for other selected Raman shifts Δ_2, Δ_3 result in similar values with 13–14 orders of magnitude CARS signal

enhancement, as can be read out from Table 1. These values exceed the single-molecule detection threshold [4] by 3 orders of magnitude.

The values given above reflect local CARS signal enhancement at the most favourable point $\vec{r}_{max}$. The spatial distribution of the enhancement factor of the Raman peak at 1314 cm^{-1} $G^{\Delta_1}(\vec{r}, \lambda_S^1, \lambda_p^1, \lambda_a^1)$ across the optimised unit cell in the xy plane directly above the nanodisks is depicted in Figure 5. Following the field enhancement profiles, SECARS signal enhancement exceeding the threshold value of 10 orders of magnitude can be achieved in the yellow regions in the gap between the nanodisks of approximate volume of 5×10^4 nm^3. This volume can hold a rhodamine molecule of approximately 1 nm in size, as well as other, potentially larger molecules.

Figure 6 depicts the field enhancement factor $FE(\vec{r}_{max}, \lambda)$ for the same metasurface geometry arrangement at the fixed position of maximum field enhancement, but depending on the illumination wavelength. The peak values can be read out from Table 1. The near-field spectrum in Figure 6
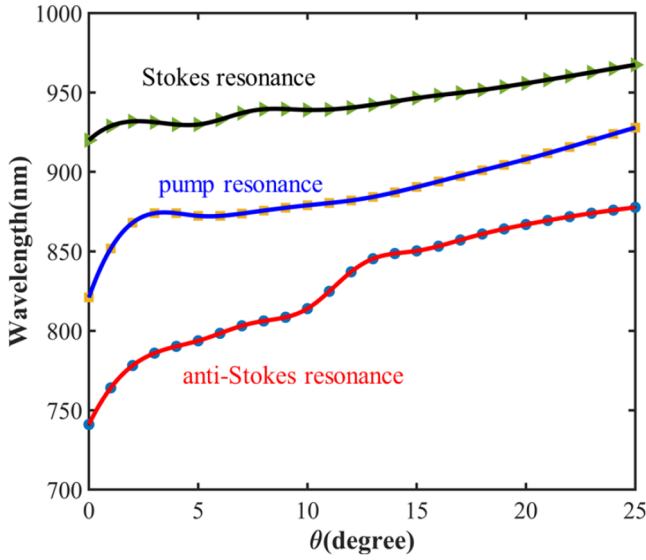
Fig. 7. Resonance wavelengths dependence on the incidence angle for the three resonance peaks of the investigated metasurface.

Fig. 8. Differences of resonance frequencies in function of the incidence angle. The crossing points correspond to fulfilling the Raman resonance condition (1) for different Raman shifts indicated in the figure.

demonstrates the broad character of the resonance peaks, in particular, of the pump and Stokes resonances. This suggests that although the metasurface geometry is now optimised for the Raman shift at $\Delta_1 = 1314$ cm^{-1}, it would still provide significant CARS signal enhancement corresponding to other prominent Raman shifts at Δ_2 or Δ_3. Indeed, the value of the CARS enhancement factor corresponding to the shift of Δ_2 sustained by the metasurface optimised for Δ_1 reaches $G^{\Delta_1}(\vec{r}_{\max}, \lambda_s^2, \lambda_p^2, \lambda_a^2) \approx 9 \times 10^{13}$. The value corresponding to the third investigated Raman shift $\Delta_3 = 1512$ cm^{-1} provided by the same nanostructure geometry is an order of magnitude smaller due to the slight mismatch with the relatively narrow anti-Stokes peak. In consequence, the structure could support Raman signal enhancement from rhodamine molecules in a broad range of a few hundred inverse centimetres around the Δ_1 shift, bringing it even 2–3 orders of magnitude above the single-molecule threshold. Similarly, the signal from other molecules could be improved with the same metasurface structure, e.g., CO_2 with the most prominent peak at 1385 cm^{-1} [26], the 1360 cm^{-1} peak of glucose [27], and many others.

Finally, please note that the investigated structure is tailored for the detection of molecules at extremely low concentrations, in particular, at the single-molecule level. The presence of molecules at such low concentrations has little influence on the refractive index of the nanoparticles' surroundings. Therefore, we expect the metasurface's optical response would hardly be modified by their presence. The molecules are rather detected with Raman techniques due to the generation of the anti-Stokes signal, absent without the molecules, therefore delivering background-free detection possibility.

3 Post-fabrication tunability

In the previous section we have demonstrated the structure's capability to improve the Raman signal in the range around
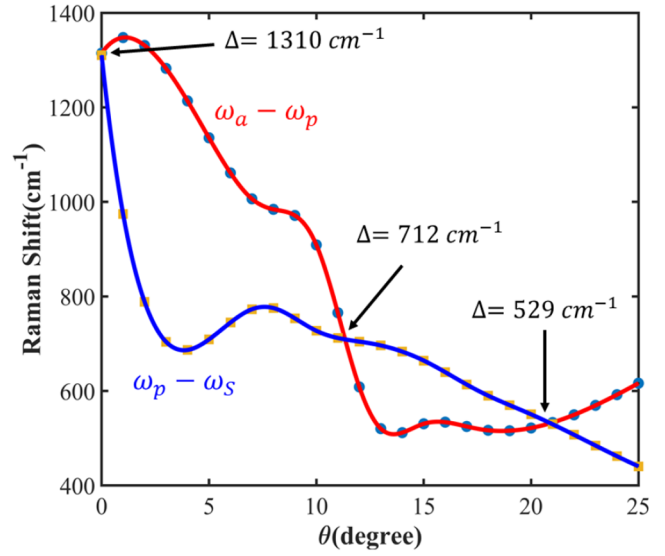
1310 cm^{-1}, with the enhancement peaks fulfilling the resonance condition (1) under normal incidence. In the MIG configuration, integration of the grating in the metasurface design provides an additional degree of freedom and a tuning knob, related to the illumination incidence angle on which the optical response of the metasurface strongly depends. The angle is denoted as θ in Figure 2. Below we demonstrate how this tunability knob can be exploited to switch between different Raman shift ranges.

Moreover, in a practical fabrication process the nano-scaled shapes, sizes and even the varying material quality are sources of imperfections that will in general degrade the achieved signal enhancement. This is typically overcome by preparing multiple samples with increasingly modified geometry parameters [28]. Here, an alternative strategy by adjustment of the illumination angle could be used instead.

We analyse the effect for the metasurface designed to match the Raman shift Δ_1 at normal incidence. As the incident angle is modified in the range from 0 to 25 deg, the resonances redshift (Fig. 7), in general breaking the CARS resonance condition (1). The differences between pairs of resonance frequencies $\omega_p - \omega_s$ and $\omega_a - \omega_p$ are shown in Figure 8, where each of the crossing points fulfils the CARS condition with a different Raman shift, in this case $\Delta = 712$ cm^{-1} for $\theta = 13°$ and $\Delta = 529$ cm^{-1} for $\theta = 21°$. This means that by changing the incident angle the resonance wavelengths can be switched from one to another Raman shift, making one metasurface operational with different molecular species.

4 Conclusions

We have discussed a MIG metasurface suitable to enhance the CARS signal, in particular from rhodamine G6, exceeding the single-particle detection threshold by up to 3 orders of magnitude.
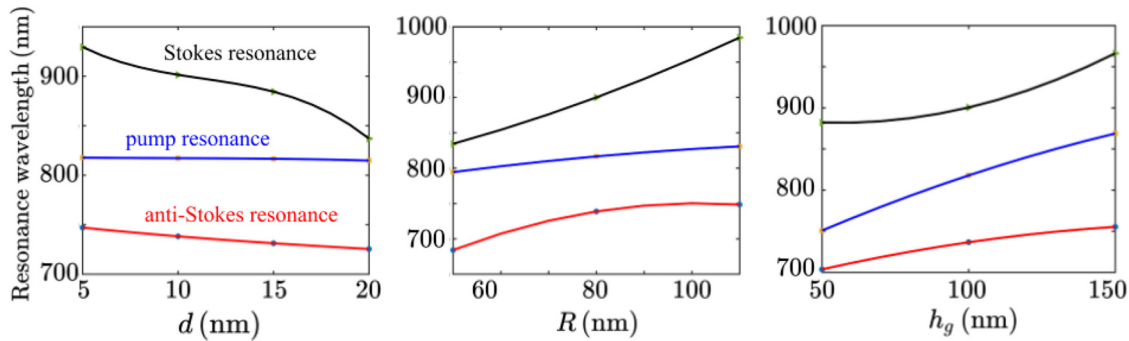
Fig. A1. Spectral position of the three investigated resonance peaks as functions of the disk geometry parameters (left: distance between nanodisks, middle: nanodisk radius) and grating height (right).

Despite the high sensitivity of the setup's spectral response with respect to its geometry parameters, especially the gap sizes, due to the broad character of the resonances the value of the SECARS enhancement factor is not crucially dependent on the very small size variation. In fact, one geometric setup arrangement can actually cover many resonances and adjust to several molecular species. Moreover, integration of the grating in the metasurface geometry makes switching between distinct ranges of Raman shifts possible by adjusting the angle at which the structure is illuminated.

Appendix A: Spectral tuning

Figure A1 presents the spectral shift of the three resonance peaks as geometry parameters of the top layer (disks) and the grating are modified. The figure corresponds to $h_d = 65$ nm, $h_s = 200$ nm, $w_g = 20$ nm, $P = 600$ nm and, unless specified differently in the figure, $R = 80$ nm, $d = 10$ nm, $h_g = 100$ nm. The figure illustrates that the positions of the two side (Stokes and anti-Stokes) resonances are sensitive to the disk parameters, while the middle pump resonance is rather robust with respect to disk geometry tuning. This is expected since the side peaks arise due to the hybridisation of the disk resonances and are absent as the disks are removed. Contrary, all three resonances red-shift as the grating height is increased, with the slightly more sensitive response of the middle peak found in the investigated range of parameters. All resonances are relatively robust to modulations of the disk height: They shift by approximately 10 nm as the disk height is scanned between 30 to 100 nm (not shown). Similarly, the spacer height being varied between 150 and 250 nm results in linear shifts of all resonances with a similar slope, weakly affecting the Raman effect.

References

1. E. Smith, G. Dent, Modern Raman Spectroscopy: A Practical Approach (John Wiley & Sons, 2019)

2. P.L. Stiles, J.A. Dieringer, N.C. Shah, R.P. Van Duyne, Surface-enhanced Raman spectroscopy, Annu. Rev. Anal. Chem. **1**, 601 (2008)

3. J.B. Jackson, N.J. Halas, Surface-enhanced Raman scattering on tunable plasmonic nanoparticle substrates, Proc. Natl. Acad. Sci. **101**, 17930 (2004)

4. E.J. Blackie, E.C. Le Ru, P.G. Etchegoin, Single-molecule surface-enhanced Raman spectroscopy of nonresonant molecules, J. Am. Chem. Soc. **131**, 14466 (2009)

5. R. Zhang et al., Chemical mapping of a single molecule by plasmon-enhanced Raman scattering, Nature **498**, 82 (2013)

6. E.C. Le Ru, P.G. Etchegoin, Single-molecule surface-enhanced Raman spectroscopy, Annu. Rev. Phys. Chem. **63**, 65 (2012)

7. C. Chen, N. Hayazawa, S. Kawata, A 1.7 nm resolution chemical analysis of carbon nanotubes by tip-enhanced Raman imaging in the ambient, Nat. Commun. **5**, 1 (2014)

8. S. Jiang et al., Distinguishing adjacent molecules on a surface using plasmon-enhanced Raman scattering, Nat. Nanotechnol. **10**, 865 (2015)

9. F. Benz et al., Single-molecule optomechanics in 'picocavities,' Science **354**, 726 (2016)

10. C. Zong et al., Plasmon-enhanced stimulated Raman scattering microscopy with single-molecule detection sensitivity, Nat. Commun. **10**, 5318 (2019)

11. R. Begley, A. Harvey, R.L. Byer, Coherent anti-Stokes Raman spectroscopy, Appl. Phys. Lett. **25**, 387 (1974)

12. M.D. Duncan, J. Reintjes, T. Manuccia, Scanning coherent anti-Stokes Raman microscope, Opt. Lett. **7**, 350 (1982)

13. A. Zumbusch, G.R. Holtom, X.S. Xie, Three-dimensional vibrational imaging by coherent anti-Stokes Raman scattering, Phys. Rev. Lett. **82**, 4142 (1999)

14. S. Lal, N.K. Grady, J. Kundu, C.S. Levin, J.B. Lassiter, N.J. Halas, Tailoring plasmonic substrates for surface enhanced spectroscopies, Chem. Soc. Rev. **37**, 898 (2008)

15. C. Steuwe, C.F. Kaminski, J.J. Baumberg, S. Mahajan, Surface enhanced coherent anti-Stokes Raman scattering on nanostructured gold surfaces, Nano Lett. **11**, 5339 (2011)

16. Y. Zhang, Y.-R. Zhen, O. Neumann, J.K. Day, P. Nordlander, N.J. Halas, Coherent anti-Stokes Raman scattering with single-molecule sensitivity using a plasmonic Fano resonance, Nat. Commun. **5**, 4424 (2014)

17. S. Yampolsky et al., Seeing a single molecule vibrate through time-resolved coherent anti-Stokes Raman scattering, Nat. Photonics **8**, 650 (2014)

18. J. He, C. Fan, P. Ding, S. Zhu, E. Liang, Near-field engineering of Fano resonances in a plasmonic assembly for maximizing CARS enhancements, Sci. Rep. **6**, 20777 (2016)

19. J. Wang et al., Theoretical investigation of a multi-resonance plasmonic substrate for enhanced coherent anti-Stokes Raman scattering, Opt. Express **25**, 497 (2017)

20. D.M. Nguyen, D. Lee, J. Rho, Control of light absorbance using plasmonic grating based perfect absorber at visible and near-infrared wavelengths, Sci. Rep. **7**, 2611 (2017)

21. S. Zhang, Y. Wang, S. Wang, W. Zheng, Wavelength-tunable perfect absorber based on guided-mode resonances, Appl. Opt. **55**, 3176 (2016)

22. E. Kirubha, P. Palanisamy, Green synthesis, characterization of Au–Ag core–shell nanoparticles using gripe water and their applications in nonlinear optics and surface enhanced Raman studies, Adv. Nat. Sci. Nanosci. Nanotechnol. **5**, 045006 (2014)

23. S. Shim, C.M. Stuart, R.A. Mathies, Resonance Raman cross-sections and vibronic analysis of Rhodamine 6G from broadband stimulated Raman spectroscopy, ChemPhysChem **9**, 697 (2008)

24. C. Tan, Determination of refractive index of silica glass for infrared wavelengths by IR spectroscopy, J. Non-Cryst. Solids **223**, 158 (1998)

25. D.P. Edward, I. Palik, Handbook of Optical Constants of Solids (Academic Press, New York, 1985)

26. G. Tejeda, B. Maté, S. Montero, Overtone Raman spectrum and molecular polarizability surface of CO_2, J. Chem. Phys. **103**, 568 (1995)

27. O. Lyandres, J.M. Yuen, N.C. Shah, R.P. VanDuyne, J.T. Walsh Jr, M.R. Glucksberg, Progress toward an in vivo surface-enhanced Raman spectroscopy glucose sensor, Diabetes Technol. Ther. **10**, 257 (2008)

28. M. Asano et al., Distillation of photon entanglement using a plasmonic metamaterial, Sci. Rep. **5**, 18313 (2015)